A Comprehensive 3-D Model on Gas Metal Arc Welding

by Junling Hu**, Hao Guo*, Guang Xu*, and Hai-Lung Tsai*

*Department of Mechanical and Aerospace Engineering
University of Missouri-Rolla, Rolla, MO 65409
**Department of Mechanical Engineering,
University of Bridgeport, CT 06604

Abstract: A unified comprehensive model was developed to simulate the transport phenomena occurring during the gas metal arc welding process. An interactive coupling between arc plasma; melting of a continuously fed electrode; droplet formation, detachment, transfer, and impingement onto the workpiece under the influences of several competing forces including gravity, electromagnetic force, arc pressure, plasma shear stress, and surface tension; and weld pool dynamics all were considered. The transient distributions of current density, arc temperature, arc pressure, melt flow velocity and melt temperature in the droplet and in the weld pool were all calculated.

Based on the unified model, the following investigations were conducted: 1) the effect of welding current on droplet generation, especially the use of pulsed current to achieve the one-droplet-per-pulse (ODPP) metal transfer; 2) the determination of dynamically stabled wire feed speeds for given welding conditions; 3) the effects of surface active elements (Marangoni effect) on the weld pool flow and solidified weld profile; 4) the fundamental mechanisms leading to the formation of ripples; 5) the issues associated with the beginning and the end of the welding (limited penetration and the formations of crater); 6) the deflection of arc plasma by an external magnetic field.

Keywords: Gas metal arc welding, Arc plasma, ODPP, Marangoni effect

1. Introduction

Due to its high productivity, the GMAW process has been the predominant welding method. The welding quality depends on various parameters, such as welding current, electrode feed speed, travel speed, and shielding gas. A comprehensive dynamic model of the GMAW process would provide many helpful insights on key process parameters leading to the improvement of weld quality. In such a model, there are three major coupling events that need to be considered: 1) the generation and changing process of arc plasma, 2) the dynamic process of droplet formation, detachment, and impingement onto the weld pool, and 3) the dynamics of the welding pool under the influences of arc plasma and the periodical impingement of droplets. Due to the complexity of the welding process, many existing numerical models simplified the process to three components: electrode, arc, and weld pool and treat each component separately. In their survey paper, Jonsson et al [1] have categorized the past, current and future arc welding modeling efforts into three generations: the first generation models are individual models (electrode model, arc model and weld pool model); the second generation models are more comprehensive models (electrode-arc model, arc-weld model and electrode-arc-weld pool model); the third generation models incorporate micromodeling of solidification and computational solid weld mechanics into the second generation models. Since Jonsson et al.'s [1] paper was published in 1994, there have been many modeling efforts in improving the first and second generation models, which paved the way for the future development of the third

generation models.

The first generation electrode models treated the electrode independent of arc. Waszink and van den Heuvel [2] presented a one-dimensional (1D) electrode model to determine the temperature distribution in a consumable electrode. They assumed the electrode to be a cylinder and only calculated the heat conduction from the electrode tip. Kim and et al. [3] developed a 2D electrode model which solved the conductive energy equation in combination with the charge-continuity equation to calculate the temperature distribution in the electrode. Choi et al. [4-5] and Wang et al. [6] presented 2D models to simulate the fluid flow inside the droplet by solving mass continuity, momentum, and current continuity equations. In their models, the electrode was considered as molten metal fed in from the top boundary. Uniform, linear or Gaussian current density distributions were assumed at the droplet surface. The droplet shape during the droplet formation was also predicted by combing the VOF method for free surface. However, the melting of the electrode was not considered. Using a similar method, Wang et al. [7] added energy equation in their 2D model and simulated both the heat transfer and fluid flow in the electrode. The droplet formation due to the melting of electrode was thus simulated.

While electrode is the unique GMAW feature, welding arc and weld pool are the shared features by gas tungsten arc welding (GTAW). GTAW had been well studied before GMAW was explored [1]. Therefore, many first or even second generation arc and weld pool models were based on the previous GTAW arc and weld pool models [8-29]. In 1993, Jonsson et al. [30] were the first to propose a 2D axisymmetrical GMAW arc model. Recently, Xu and Tsai [31] developed a 3D GMAW arc model. The approach they used in their model is essentially the same as that in the GTAW arc models, but the intrinsic differences between the two processes were considered. In their models, the transport phenomena in the arc column were simulated by solving mass continuity, momentum, energy and current continuity equations together. The non local thermodynamic equilibrium (LTE) conditions at the anode and cathode fall regions were considered through boundary conditions. The electrode was considered to be a cylinder, thus, electrode tapering and melting were not taken into account.

Before the first GMAW weld pool model was published by Tsao and Wu [32] in 1988, many GTAW weld pool models have been developed [17-29]. Tsao and Wu's 2D weld pool model simulated the convection in a stationary weld pool and considered the impingement of metal droplets onto the weld pool by the thermal energy exchanged. The weld pool surface was assumed to be flat in their model. Zacharia et al. [33] presented a 3D weld pool model which accounted for the deformation of free surface by using the surface elevation as a solution variable for the finite-difference grids of the surface layer. The rate of filler-metal addition was specified at the melt surface. Tekriwal and Mazumder [34] presented a 3D moving source heat transfer analysis by expanding the finite element mesh in time to accommodate the metal transfer. Kumar and Bhaduri [35-36] presented a 3D heat conduction model where the heat energy delivered due to the metal transfer had been approximated in the form of a cylindrical volumetric heat source. Kim and Na [37-38], Kim et al. [39], and Ohring and Lugt [40] used boundary fitted coordinates to incorporate the weld pool surface deformation, but the effect of droplet was ignored in the first two models and treated as liquid column in the third model. The dynamic change of the weld pool free surface later was modeled by Wang and Tsai [41-42] and Fan and Kovacevic [43-44] using the VOF method and Cao et al. [45] using the FAVOR method. In spite of the differences in modeling weld pool surface deformation and droplet impingement, these first generation weld pool models all simultaneously solved the coupled momentum, energy, and continuity equations by assuming current density, momentum, and energy boundary conditions at the weld pool surface.

Considerable advances have been made in modeling the electrode, arc and weld pool over the last decades. The advances made from the individual components have allowed these separate components to be integrated into a more comprehensive system. Depending on the degree of coupling between the individual components, the second generation GMAW models include electrode-arc models and electrode-arc-weld pool models. Zhu et al. [46] presented an electrode-arc model by combing an arc model with a 1D conduction model for the moving electrode. The non-LTE effects in the anode boundary was simplified and only conductive heat transfer across the electrode was taken into account. The heat input to the electrode was estimated from the arc plasma, and the 'molten' metal was discarded when its temperature reached the melting point. Haidar and Lowke [47] and Haidar [48] presented a similar arc-electrode model to simulate the droplet formation in GMAW. The mass continuity, momentum, energy equations were solved in the electrode to simulate the heat transfer and fluid flow in the electrode. VOF method was used to track the deformed free surface of the electrode. The droplet formation and detachment were simulated by considering the dynamic interaction of the arc plasma and the droplet. Haidar [49-51] further developed this GMAW model to take into account the sheath effect at the anode surface. However, in all the above mentioned arc-electrode models, the droplets were eliminated immediately when they were detached from the electrode tip. The weld pool dynamics was also neglected and the workpiece was treated as a flat plate. The fluid flow in the weld pool was not calculated and only conduction was considered. Zhu et al. [52] and Fan and Kovacevic [53] have first attempted arc-electrode-weld pool models. However, the simulated arc plasma distributions matched both the experimental results [43-44,54-56] and the simulation results from aforementioned arc models [8-16,46-51] poorly. The arc plasma flow in Fan and Kovacevic's model [53] could not push the detached droplets down and an empirical formulation was used to calculate the plasma drag force. Recently, Hu and Tsai [57-59] developed a 2D comprehensive arc-electrode-weld pool model which can simulate the interactive coupling between arc plasma; melting of the electrode; droplet formation, detachment, transfer, and impingement onto the workpiece; and weld pool dynamics.

Based on the previous models developed by the authors [31,42,57-61], the following investigations were conducted: 1) the effect of welding current on droplet generation, especially the use of pulsed current to achieve the one-droplet-per-pulse (ODPP) metal transfer; 2) the determination of dynamically stabled wire feed speeds for given welding conditions; 3) the effects of surface active elements (Marangoni effect) on the weld pool flow and solidified weld profile; 4) the fundamental mechanisms leading to the formation of ripples; 5) the issues associated with the beginning and the end of the welding (limited penetration and the formations of crater); 6) the deflection of arc plasma by an external magnetic field. The mathematical formulations can be found in our previous papers [31, 42, 57-60] and are not repeated here.

2. Results and Discussions

2.1 The effects of welding current on metal transfer

Current is one of the most important factors that affect the droplet formation. In this section, the effects of current on metal transfer were studied with five welding currents, including two constant currents and three pulsed currents. The detailed information of the mathematical modeling and welding conditions can be found in Ref. [58].

Figure 1 shows the temperature distributions for three currents, including two constant

currents at 175 A and 280 A and the first pulsed current with an average current of 175 A. At a constant current of 175 A, as shown in Fig. 1(a), the droplet is detached from the electrode tip with an average diameter of 3.2 mm. The droplet detachment frequency is less than 5 Hz. As the electromagnetic force is small at low currents, the droplet is detached by the competition of surface tension and gravity force. At a high current level, the electromagnetic force plays a major role in pinching the droplet off the electrode tip. In Fig. 1(b), he average diameter of the detached droplets at 280 A is 1.4 mm and the detachment frequency is 90 Hz. In the case of pulsed current as shown in Fig. 1(c), the high peak current pinches the droplet off the electrode with the controlled pulse frequency 20 Hz. The detached droplets have an average diameter of 1.9 mm.

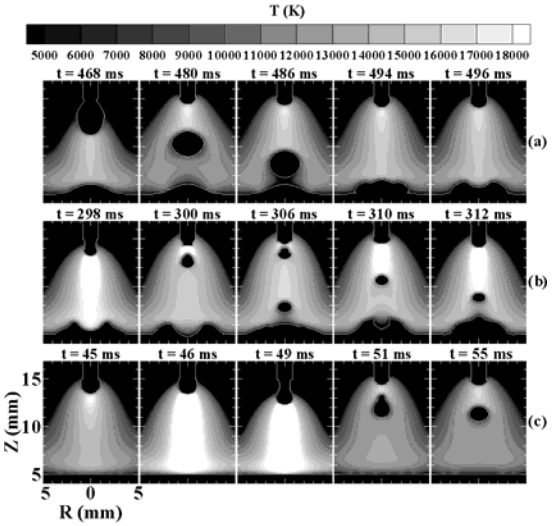

Fig. 1 Temperature distributions for three currents: (a) the 175A constant current, (b) the 280 A constant current, (c) the pulsed current with an average current of 175 A.

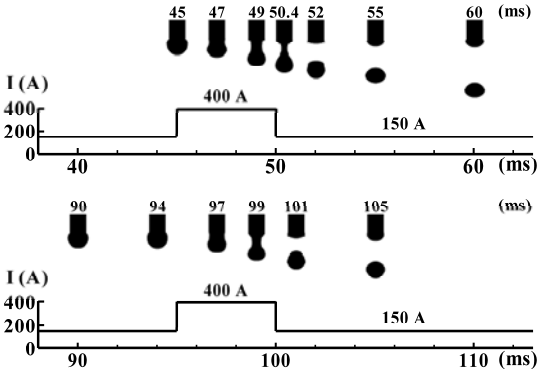

Fig. 2 Droplet profiles during the metal transfer process with a pulsed current of 5 ms peak duration.

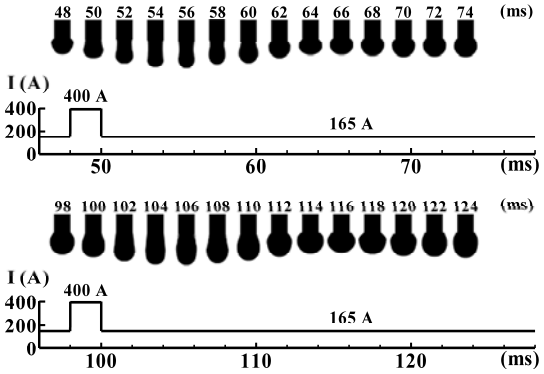

Fig. 3 Droplet profiles during metal transfer process with a pulsed current of 2 ms peak duration.

One droplet per pulse (ODPP) metal transfer mode is the desirable metal transfer mode with the advantages of low average currents, a stable and controllable droplet generation, and reduced spatter. With three pulsed currents of different peak durations, the effect of peak current duration on achieving ODPP is studied in the following figures. Figure 2 shows the dynamic droplet development and detachment process of the first pulsed current with peak duration of 5 ms. One droplet is detached during the peak durations and no other droplet is detached in the following base duration. Thus, one

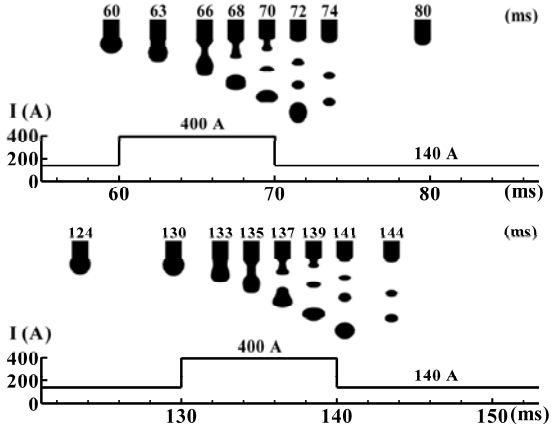

Fig. 4 Droplet profiles during metal transfer process for a pulsed current of 10 ms peak duration.

droplet is detached at the end of peak current for each pulse. As it is shown in Fig. 3, the 2 ms peak duration is insufficient to detach the droplet from the electrode tip and the subsequent current pulse also fails to detach the growing droplet. The increased electromagnetic force in the short peak duration elongates the droplet. The surface tension force bounces the droplet back after the peak duration. The increased electromagnetic force during the second pulse peak duration pinched the liquid metal to flow downward from t = 100 ms. However, the pinch effect is even smaller on the liquid metal as the droplet becomes bigger now than in the first pulse. When the peak duration is too long, the undesirable multiple droplets per pulse occurs. As shown in Fig. 4, three droplets are detached in each pulse for peak duration of 10 ms. After a droplet is detached, the remaining fluid is pinched off by the high electromagnetic force with a form of two subsequent small droplets.

2.2 The effects of wire feed speed

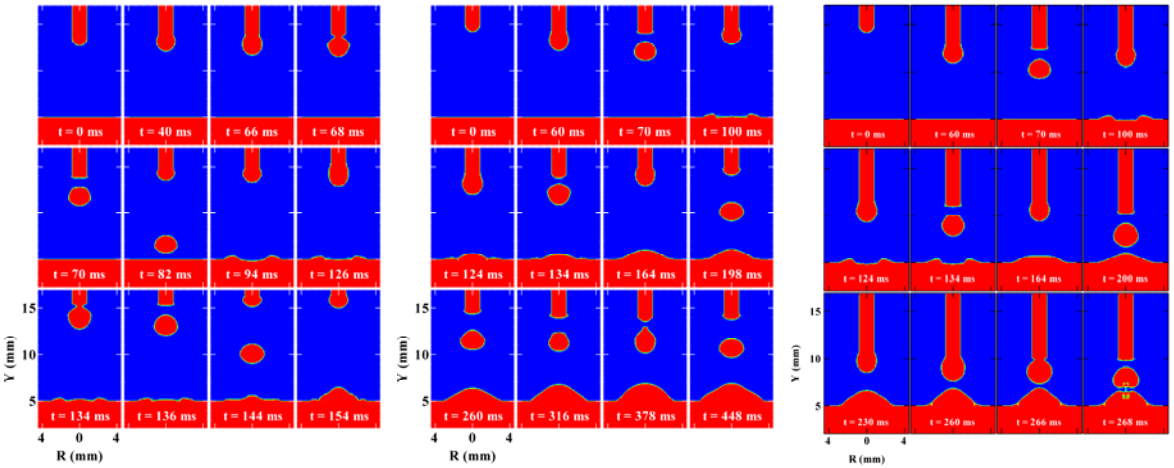

(a) (b) (c)

Fig. 5 A sequence of droplet detachment positions: (a) v = 4 cm/s; (b) v = 6 cm/s; (c) v = 8 cm/s.

In a GMAW process, filler metal is supplied by consumable electrode. The electrode is heated and molten, and droplets are formed and detached at the tip of the electrode. For a stable welding process, the wire feed speed must be equal to the wire melting rate. If the wire feed speed is less than wire melting rate, the electrode would be burnt back, and if the wire feed speed is greater than the wire melting rate, the electrode will insert into the weld pool and the welding arc will extinguish or severe spattering occurs when the electrode short-circuits the weld pool. The wire feed speed recommended by the welding handbook [62] is 5.9 cm/s for a mild steel electrode with a 1.6 mm diameter at 240 A. In this section, three cases are simulated to study the effects of wire feed rate. The electrode is mild steel with a diameter of 1.6 mm and the welding condition is constant current at 240 A. Three different wire feed speeds are chosen as 4 cm/s, 6 cm/s and 8 cm/s. All the other welding parameters are set the same, except the original electrode extension is set 1 mm longer for the first case. A sequence of droplet formation and detachment positions for each case is shown in Fig. 5.

As shown in Fig. 5(a), the electrode tip position moves up form Y = 12.7 mm at t = 0 ms, to Y = 13.8 mm at t = 70 ms after the detachment of the first droplet, and Y = 15.3 mm at t = 136 ms after the detachment of the second droplet. Thus, it can be seen clearly that the electrode melts faster than the wire feed speed of 4 cm/s. For case two, six droplet detachments are shown in Fig. 5(b). The electrode tip position after the first droplet detachment

is Y = 14.0 mm. For the 2nd, 3rd, 4th, 5th, and 6th droplet, the electrode tip positions after the droplet detachment are Y = 13.9 mm, 14.1 mm, 14.2 mm, 14.0 mm, 13.6 mm and 13.7 mm. The range of these positions is very narrow, thus it is reasonable to assume this case is stable at 6 cm/s, which is close to the recommended wire feeding speed of 5.9 cm/s. For case three shown in Fig. 5(c), the wire feed speed is 8 cm/s. The electrode tip position shortly before the first droplet is detached is Y = 11.0 mm. For the 2nd to 4th droplets, the electrode positions shortly before the detachment are Y = 9.4 mm, 8.1 mm and 7.8 mm. There is clearly a trend for the electrode to continuously move down to the weld pool. As seen in Fig. 5(c), the droplet tip almost touches the weld pool at t = 266 ms. Then, at t = 268 ms, the droplet has been detached from the electrode and also rejected from the weld pool due to the short-circuiting effect happened between t = 266 ms and t = 268 ms.

2.3 The effects of surface active elements

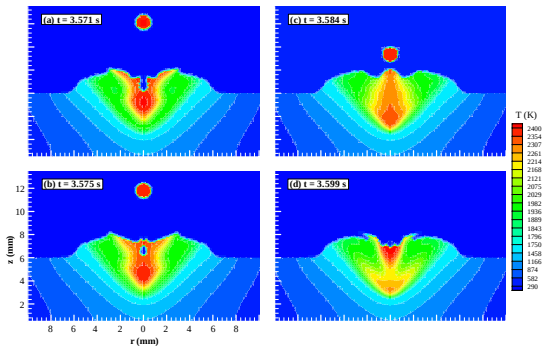

Fig. 6 A typical sequence of droplet impinging onto the weld pool and temperature distributions; droplets S = 300 ppm, base metal S = 100 ppm.

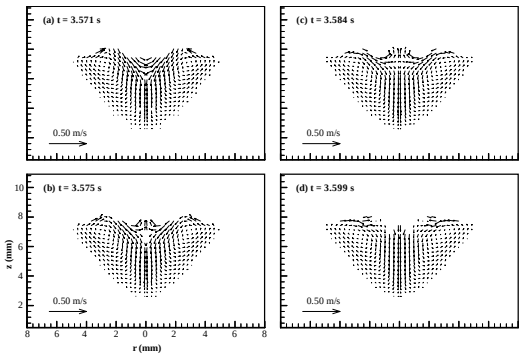

Fig. 7 The weld pool velocity distributions corresponding to Fig. 6.

In this section, two representative sulfur concentrations for the droplet were selected to study the effects of surface active elements, 300 ppm (Case I) and 150 ppm (Case II). Both the base metal and the droplets are assumed to be 304 stainless steel and the sulfur concentration in base metal is assumed to be 100 ppm. A typical sequence of a droplet impinging onto the weld pool and the temperature, and velocity distributions in the weld pool are shown in Figs. 6-9 for both cases. More figures and modeling information can be found in [42].

A. *Case I: Droplets Containing Higher Sulfur, S = 300 ppm*

In Fig. 6, it is clearly seen that the "hot" droplet carries high thermal energy sinking to the bottom of the weld pool in which the thermal energy is dissipated. The fluid flow pattern in the weld pool, as shown in Fig. 7, is generally downward along the center of the weld pool and then upward along the liquid-solid interface, creating a counter clockwise vortex.

The flow pattern, shown in Fig. 7, results mainly from the inward surface tension force. Near the weld pool center with a radius of about 1.0 mm, the temperature of the weld pool surface is 2300~2400 K, while the sulfur concentration is 250~300 ppm. As both the temperature and the sulfur concentration at the weld pool surface decrease outward, the surface tension force in this central area is radically outward. However, away from the center of the weld pool, the surface temperature is below 2100 K and the sulfur concentration is below 210 ppm, leading to a negative Marangoni shear force (i.e., inward). Note the outward surface

tension force described above exists only in a small portion of the surface around the center of the weld pool, while the inward force prevails over most of the weld pool surface. The falling droplet creates a downward fluid flow near the weld pool center. In addition, the electromagnetic force produces an inward and downward flow. Due to the interaction among the aforementioned forces, the resulting surface-tension-driven (Marangoni) flow is radially inward. The inward flow brings the higher temperature surface fluid downward to the bottom of the weld pool, leading to a deeper penetration.

B. *Case II: Droplets Containing Lower Sulfur, S = 150 ppm*

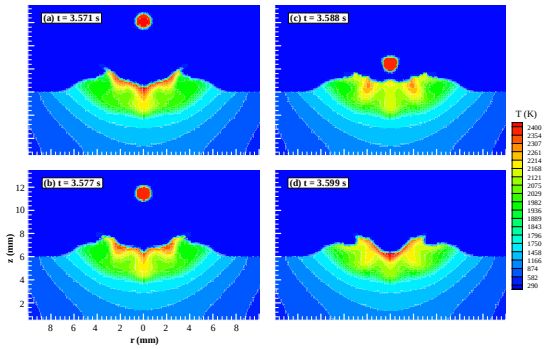

Fig. 8 A typical sequence of droplet impinging onto the weld pool and temperature distributions; droplets S = 150 ppm, base metal S = 100 ppm.

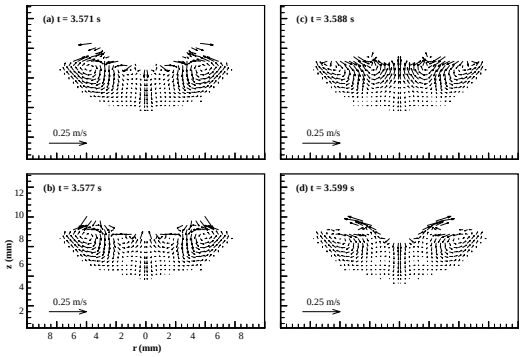

Fig. 9 The weld pool velocity distributions corresponding to Fig. 8.

As shown in Fig. 8, the shape of the isotherm curves near the weld pool center is quite complex and different from that in Case I. There are two visible vortexes; clockwise near the weld pool center and counter clockwise near the edge of the weld pool, Fig. 9(b). In this case, the area near the weld pool center has a sulfur concentration of 140~150 ppm. However, the surface temperature near the weld pool center is 2300~2400 K and decreases outward to the edge of the weld pool. As a result, the maximum surface tension occurs in the middle of the weld pool surface, pulling surface fluid from both the center and the edge toward the middle of the weld pool. Hence, there is a downward flow in the middle of the weld pool surface.

The flow pattern is influenced mainly by the interaction of two forces; electromagnetic force and the droplet impinging momentum. The electromagnetic force is inward and downward which may weaken the outward flow by surface tension near the weld pool center. The momentum carried by the droplet rebounds resulting in a strong upper flow at the center of the weld pool, Fig. 9(c). The fluid near the center of the weld pool flows downward due to both the electromagnetic force and the falling momentum of the droplet.

As the surface fluid flow outward near the center of the weld pool, the thermal energy from the arc flux is spread outward. In addition, the thermal energy carried by the droplets does not effectively carry down to the weld pool, as compared to Case I. As a result, the weld pool is shallow but wider, as compared to Case I.

C. *Final Weld Bead Shape after Solidification*

After the last droplet is released, the arc power is turned off at t = 4.00 s. Figure 10 shows the sulfur concentration distribution and the shape of the weld bead after full solidification in Cases I and II. As shown, the weld bead has a deeper penetration but is a little narrower in Case I as compared to Case II. The final sulfur concentration distribution in the weld bead appears to be fairly uniform for both Case I and Case II, except in regions near

the bottom and the edge of the weld pool and along the heat-affected-zone. This is caused by the fact that in these regions, the mixing of fluid is more limited. The predicted uniform sulfur distribution is consistent with the published experimental observation for the cases when two dissimilar metals are welded together or the compositions of electrodes are different from the base metal [63].

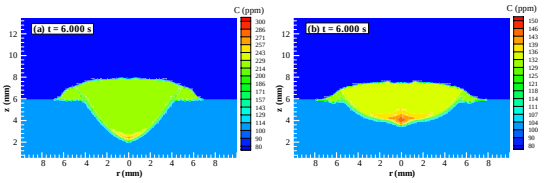

Fig. 10 Final shape of the weld pool and sulfur concentration distribution when the droplet sulfur concentration is (a) S = 300 ppm; (b) S = 150 ppm.

2.4 The formation of ripples

Ripples left in the solidified weld bead, as shown in Fig. 11, are very common in gas metal arc welding. Understanding the mechanisms leading to the formation of ripples will be helpful in determining the weld bead shape, including undercut and overlap which can affect weld quality. In this section, the distributions of temperature and flow pattern for a moving GMAW for 304 stainless steels were calculated and shown in Figs. 12 to explain the formation of ripples.

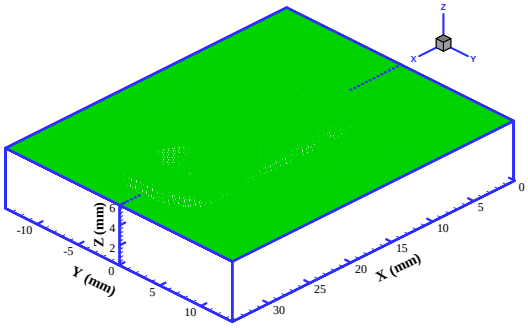

Fig. 11 Partial view of the three-dimensional mesh system and deposition height at t = 2.564 s.

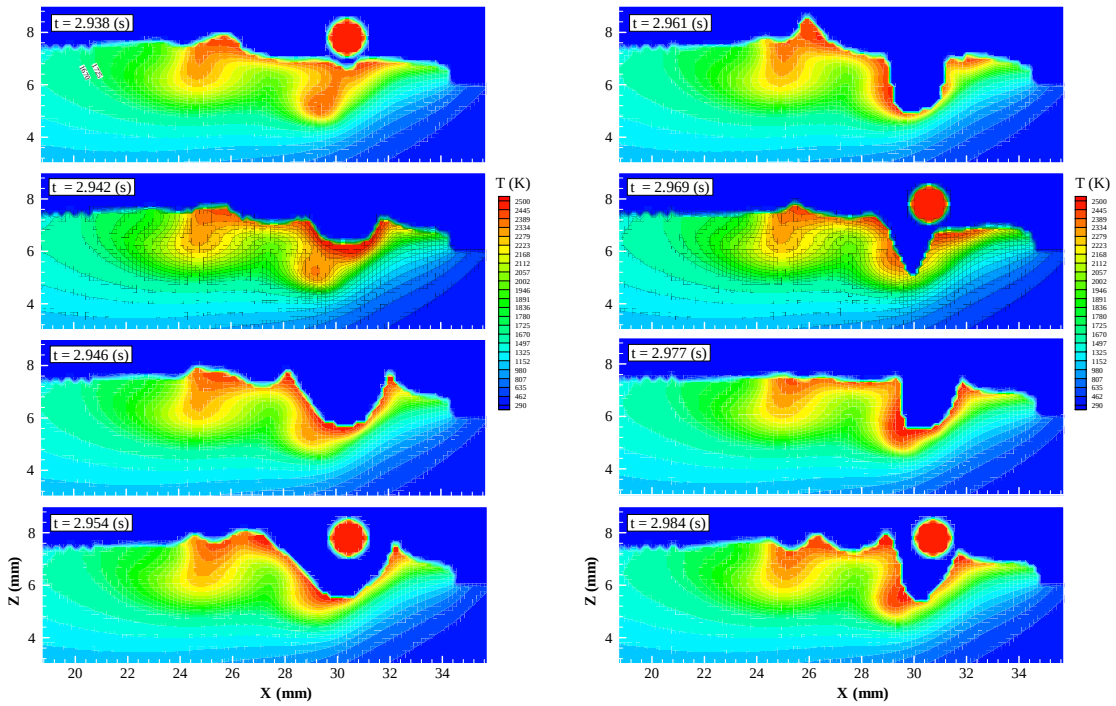

Fig. 12 A typical sequence showing the impinging process, weld pool dynamics, and temperature distributions (side view).

Figure 11 is a partial view of a three-dimensional mesh system and weld deposition at t =

2.564 s. As indicated from the figure, there are some distinct ripples in the solidified weld puddle, two moving "waves" in the molten weld pool and a "crater" caused by the impinging droplet at that instant of time. At t = 2.938 s in Fig. 12, there are four ripples which have been formed (i.e., solidified) while the liquid level of the weld pool next to the ripples is as high as that of the "tip" of the ripples. It is noted that the isotherm 1725 K shows the liquidus line, while the curve of 1670 K indicates the solidus line. As seen at t = 2.938 s, the liquidus line reaches nearly the same height as that of the tip of the ripples. The mechanisms leading to the formation of a ripple can be summarized as follows. First, due to droplet impingement, a crater is created pushing the fluid upward and away from the arc center. A wave with its peak height greater than the liquid level is also generated, propagating outward. Second, due to hydrostatic force, the high-level fluid tends to fill up the crater and decreases the liquid level. Third, as welding proceeds in the right-hand direction, solidification also moves in the same direction. As high-level fluid near the tail edge is solidified before moving down and flowing back in the crater direction, a ripple is created. Hence, the formation of ripples is related to the open and close-up of the crater and the resulting up-and-down of the weld pool fluid level. The time required for the up-and-down cycle for fluid level near the tail edge and the "pitch" of the ripples depends on many welding parameters, including droplet size (electrode diameter), droplet momentum, drop frequency (wire feed speed), welding speed, welding power (current and voltage), and others. It is noted that all these welding parameters and conditions are coupled together.

The detailed explanation of ripple formation mechanism can be found in Ref. [61].

2.5 The end effects at the beginning and the end of the welding

At the beginning stage of the welding, when the metal is still "cold", which is frequently called cold weld, limited weld penetration occurs. On the other hand, at the ending stage of the welding, a "crater" is formed which often involves micro-cracks and micro-pores. In this section, the formations of the cold weld and crater for GMAW of 6005-T4 aluminum alloy were calculated. The detailed study can be found in Ref. [60]

A. *Cold weld at the beginning of the welding*

Figures 13-14 are side views of the initial stage of the welding process showing the weld bead shape change and temperature field distribution, respectively.

It can be observed that at the beginning of the welding process, since the heat input is not enough to melt the solid metal and the thermal diffusivity of aluminum alloy is very high, the deposited material solidifies and forms a welding spot on the base metal surface. At t = 0.02 s after the welding process was initiated, several droplets have impinged onto the work piece plate. The bulk metal is still at a temperature close to room temperature except for the area beneath and around the welding arc. The heat is conducted away very fast due to the high thermal conductivity of aluminum alloy and the liquid solidifies very quickly once it impinges onto the solid metal surface. At this moment, the heat provided by the additional several droplets and welding arc is neither enough to melt the base metal nor sufficient to re-melt the previously solidified material. Therefore, the droplets solidify and overlap with each other and a small hump is formed under the arc center.

As the welding process continues, the temperature of metal increases, which melts both the weld bead metal and workpiece. A weld pool with a crater shaped surface is formed due to the combined effect of arc pressure, surface tension and impingement of droplet. Therefore,

the weld pool surface is depressed, penetration of the weld increases. While the weld pool moves to the positive x direction with arc center, it solidifies at the rear end and forms the weld bead.

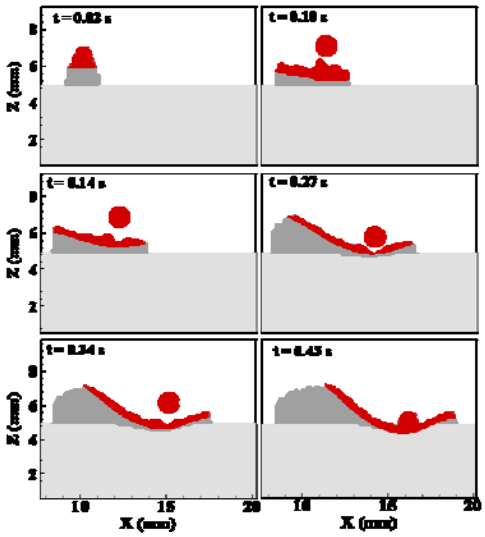

Fig. 13 Side view of formation of weld bead. The region with darkest color is weld pool. The second darkest region is weld bead.

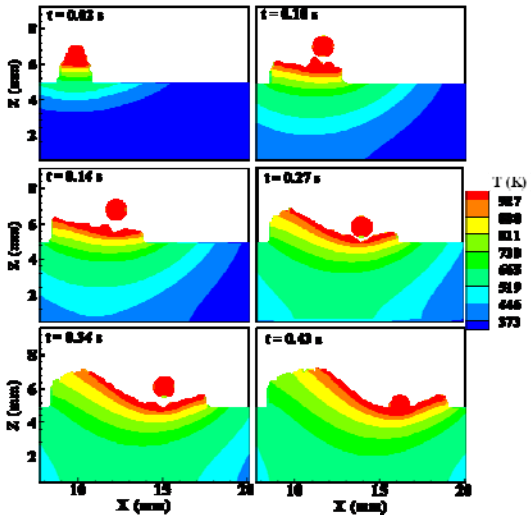

Fig. 14 Side view of weld formation showing temperature field.

B. *Crater at the end of the welding*

Figure 15 shows a partial three dimensional view of the simulated weld crater. Figures 16 and 17 are side views of the ending of the welding process showing the temperature field and velocity distribution, respectively. Before the arc is terminated at t = 1.4 s, a weld pool has already been formed and the fluid in the weld pool flows away from the arc center. A weld pool with a crater shaped surface is formed due to this flow pattern. The outward flow and the weld pool surface profile are maintained by the combined effect of arc pressure, surface tension and impingement of droplet. At t = 1.4 s, the arc is terminated and there is no heat input and material transfer into the weld pool. The heat is transferred away from the weld pool via conduction to the bulk metal, convection between the liquid metal and air, and radiation loss to the surrounding environment. The weld pool begins to solidify as the result of heat dissipation. Since droplet impingement and the arc pressure do not exist anymore, there is no force at the arc center to depress the weld pool free surface and push the fluid to flow downward and outward. The molten metal tends to flow back under the gravity force. However, because the solidification is very fast, there is no time for the liquid to flow back and fill the crater. After the weld pool fully solidifies within 0.004 s, a weld bead cross section is formed with a crater at the center.

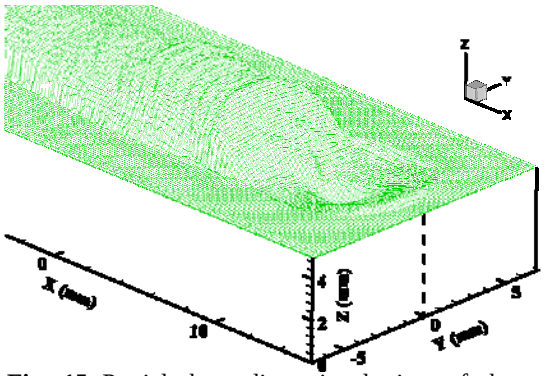

Fig. 15 Partial three dimensional view of the simulated weld crater.

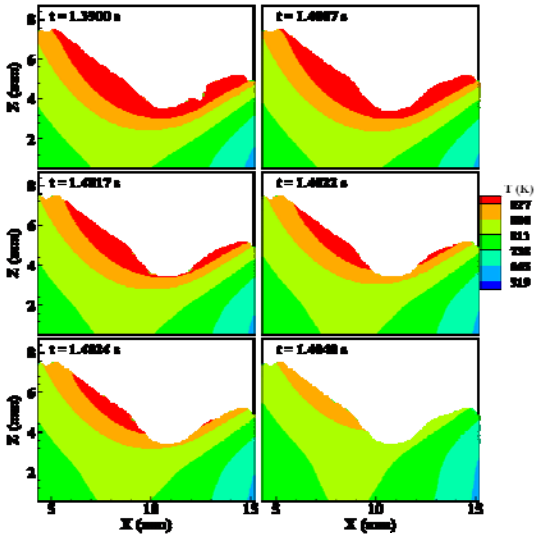

Fig. 16 Side view of formation of crater showing temperature field.

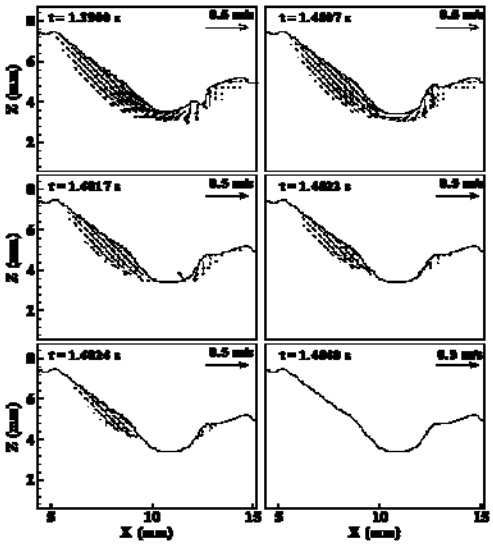

Fig. 17 Side view of formation of crater showing velocity distribution

2.6 The deflection of arc plasma

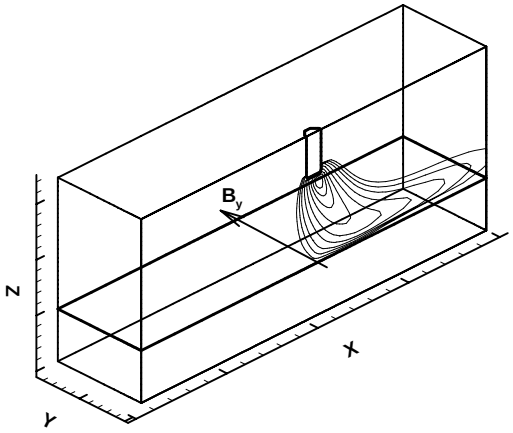

Fig. 18 A schematic representation for arc deflection.

A schematic representation of the arc deflection is shown in Fig. 18, where an external magnetic field exists. According to [64], the external magnetic fields can be caused by residual magnetism in ferromagnetic materials or external electric current. They are uncontrollable, but in some cases an external magnetic field may be applied on purpose to control the plasma deflection for a better welding quality [65]. In the present study, a uniform 35 Gauss (0.0035 Tesla) external magnetic is applied

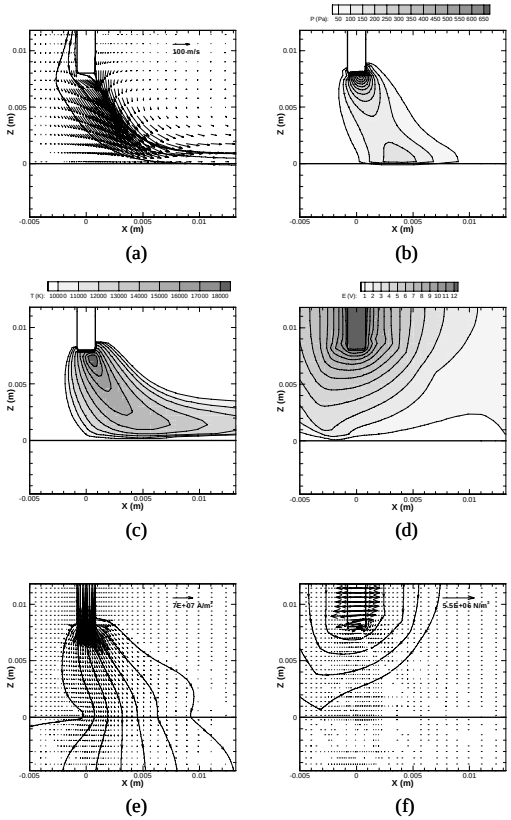

Fig. 19 Two-dimensional vectors with streamlines or distributions for the deflected arc at the symmetric plane (y = 0) for (a) velocity, (b) pressure, (c) temperature, (d) electric potential, (e) electric current density, and (f) electromagnetic force.

in the positive *y* direction. A 3-D arc model is used to simulate the arc deflection. The detailed study can be found in Ref. [31].

Figs. 19(a)-(f) show the two dimensional plots for the deflected arc. The plasma arc deflects from the axis to the positive *x* direction and the arc length is therefore elongated. This is caused by the deflection of plasma flow, which is in turn driven by the electromagnetic force from both the self-induced and the external applied magnetic fields. The maximum flow velocity decreases to 203 m/s in comparison with 264 m/s for the axisymmetric case, and the maximum arc temperature drops to 18,840 from 21,550 K. The high pressure region on the workpiece drifts with the deflected arc and the maximum pressure is 132 Pa, while this value for the axisymmetric arc is 604 Pa. The electric potential (voltage) increases to 12.7 V, a 0.3 V augment from the previous case. All these differences are the effects of the elongated plasma arc. The electric current also drifts with the deflected arc and the electromagnetic force at the electrode tip is not axisymmetric again. In the GMAW process, the unbalanced electromagnetic force may taper droplets to a deflected globular shape. The deflected droplets can be seen from many GMAW photographs [54]. One possible account might be the external magnetic perturbations.

3. Conclusions

Based on the previous models developed by the authors [31,42,57-60], some interesting phenomena in the GMAW processes were simulated. From the simulation results, the following conclusions could be draw:

(1) Smaller droplet size and higher droplet frequency were found with higher currents under the constant current conditions. However, small droplet size and high droplet frequency can be obtained with a pulsed current at a low average current level. With the appropriate control of pulse shape, one-droplet-per-pulse (ODPP) metal transfer can be achieved.

(2) For a stable gas metal arc welding (GMAW) process, the wire feed speed must be equal to and in dynamic equilibrium with the wire melting rate, which depends on several welding parameters, such as welding current, wire diameter, and wire material. With the simulation tools, a dynamically stabled wire feed speeds for given welding conditions can be obtained.

(3) Complicated fluid flow in the weld pool is influenced by the droplet impinging-momentum, electromagnetic force, natural convection due to temperature and concentration gradients, and surface tension, which is a function of temperature and concentration of a surface active element. With different concentration of surface active elements, different weld pool fluid flow pattern, weld pool size, and weld penetration depth, and solidified weld pool profile can be obtained.

(4) The formation of a ripple is closely related to the dynamic behavior of a crater formed by droplet impingement in a GMAW process. The open and close-up of the crater and the resulting up-and-down of the weld pool fluid level together with the solidification after the moving arc are the causes of the formation of ripples.

(5) At the beginning stage of the welding, when the metal is still “cold”, which is frequently called cold weld, limited weld penetration occurs. On the other hand, at the ending stage of the welding, a “crater” is formed which often involves micro-cracks and micro-pores. The lack of penetration in cold weld is due to quick solidification of the droplets at the “cold” metal plate. The crater formation is caused by rapid solidification of the weld pool when the welding arc is terminated.

(6) A non-axisymmetric plasma arc caused by an external magnetic field was studied. The

computational results show the deflection and other changes of plasma arc under the effect of an external magnetic field.

References

1) P.G. Jonsson, J. Szekely, R.T.C. Choo, and T.P. Quinn: *Modeling Simul. Mater. Sci. Eng.*, **2** (1994), p. 995.
2) J.H. Waszink and G.J.P.M. van den Heuvel, *Arc Physics and Weld Pool Behaviour (Cambridge: The Welding Institute)*, 1979, p. 227.
3) Y.S. Kim, D.M. McKelligot and T.W. Eagar, *Weld. J.*, **70** (1991), p.20s.
4) S.K. Choi, C.D. Yoo and Y.S. Kim, *Welding J.* (1998), p. 38s.
5) S.K. Choi, C.D. Yoo and Y.S. Kim, *Welding J.* (1998), p. 45s.
6) G. Wang, P.G. Huang and Y.M. Zhang, *Metall. Trans.* **34B** (2003), p. 345.
7) F. Wang, W.K. Hou, S.J. Hu, E. Kannatey-Asibu, W.W. Schultz and P.C. Wang, *J. Phys. D: Appl. Phys.*, **36** (2003), p. 1143.
8) J.J. Lowke ,*J. Appl. Phys.*, **50**(1979), p. 147.
9) S. Ramakrishnan and B. Nuon, *J. Phys. D: Appl. Phys.*,**13** (1980), p. 1845.
10) C.J. Allum, *J. Phys. D: Appl. Phys.*, **14** (1981), p. 1041.
11) K.C. Hsu, K. etemadi and E. Pfender, *J. Appl. Phys.*, **54** (1983), p. 1293.
12) K.C. Hsu and E. Pfender, *J. Appl. Phys.*, **54** (1983), p. 3818.
13) P. Kovitya and J.J. Lowke, *J. Phys. D: Appl. Phys.*, **18** (1985), p. 53.
14) P. Kovitya and L.E. Cram, *Weld. J.*, **65** (1986), p. 34.
15) P. Tekriwal and J. Mazumder, *Met. Construction*, **20** (1988), p. 275R.
16) M.C. Tsai and S. Kou, *Int. J. of Heat Mass Transf.*, **33** (1990), p. 2089.
17) G.M. Oreper, T.W. Eagar and J. Szekely, *Weld. J.*, **62** (1983), p. 307s.
18) G.M. Oreper and J. Szekely, *Fluid Mech.*, **147** (1984), p. 53.
19) S. Kou and D.K. Sun, *Metall. Trans.* **16A** (1985), p. 203.
20) G.M. Oreper, J. Szekely and T.W. Eagar, *Metall. Trans.*, **17B** (1986), p. 735.
21) A Matsunawa, S. Yokoya and Y. Asako, *Trans. JWRI*, **16** (1987), p. 1.
22) M.E. Thompson and J. Szekely, *Int. J. Heat Mass Transf.*, **32** (1989), p. 1007.
23) G.M. Oreper and J. Szekely, *Metall. Trans.*, **18A** (1987), p. 1325.
24) T. Zacharia, S.A. David, J.M. Vitek and T. Debroy, *Weld. J.*, **68** (1989), p. 499s.
25) T. Zacharia, S.A. David, J.M. Vitek and T. Debroy, *Weld. J.*, **68** (1989), p. 510s.
26) T. Zacharia, S.A. David, J.M. Vitek, **Metall. Trans.**, **22B** (1991), p. 233.
27) T. Zacharia, A.H. Eraslan and D.K. Aidun, **Weld. J.**, **67** (1988), p. 53s.
28) T. Zacharia, A.H. Eraslan, D.K. Aidun and S.A. David, *Metall. Trans.*, **20B** (1989), p. 645.
29) S. Kou and Y.H. Wang, *Metall. Trans.*,**17A** (1986), p. 2271.
30) P.G. Jonsson, R.C. Westhoff and J. Szekely, *J. Appl. Phys*, **74** (1993) p. 5997.
31) G. Xu and H.L. Tsai, *Proc. International Mechanical Engineering Congress and Exposition*, Illinois (USA), American Society of Mechanical Engineering, Nov. 5-10 (2006).
32) K.C. Tsao, C.S. Wu, *Weld. J.*, (1988) 70s-75s.
33) T. Zacharia, A.H. Eraslan and D.K. Aidun, *Weld. J.*, **67** (1988), p. 18s.
34) P. Tekriwal and J. Mazumder, *Weld. J.*, **67** (1988), p. 150s.
35) S. Kumar and S.C. Bhaduri, *Metall. Trans.*, **25B** (1994), p. 435.
36) S. Kumar and S.C. Bhaduri, *Metall. Trans.*, **26B** (1994), p. 611.
37) J.W. Kim and S.J. Na, *Weld. Joining Proc.*, **51** (1991), p. 159.
38) S.D. Kim and S.J. Na, *Welding J.*, **74**, p. 141s.
39) C.H. Kim, W. Zhang and T. DebRoy, *J. Appl. Phys.*, **94** (2003), p. 2667.
40) S. Ohring and H.J. Lugt, *Welding J.*, (1999), p. 416.

41) Y. Wang and H.L. Tsai, *Int. J. Heat Mass Transfer*, **44** (2001), p. 2067.
42) Y. Wang and H.L. Tsai, *Metall. Trans.*, **32B** (2001), p. 501.
43) H.G. Fan and R. Kovacevic, *Metall. Trans.*, **30B** (1999) p. 791.
44) H.G. Fan and R. Kovacevic, *J. Phys. D: Appl. Phys.*, **31** (1998) p. 2929.
45) Z. Cao, Z. Yang and X.L. Chen, *Welding J.*, (2004), p. 169s.
46) P. Zhu, M. Rados and S.W. Simpson, *Plasma Sources Sci. Technol.*, **4** (1995), p. 495.
47) J. Haidar, J.J. Lowke, *J. Appl. Phys. D: Appl. Phys.*, **29** (1996), p. 2951.
48) J. Haidar, *J. Phys. D: Appl. Phys.*, **31** (1998), p.1233.
49) J. Haidar, *J. Appl. Phys.*, **84** (1998), p. 3518.
50) J. Haidar, *J. Appl. Phys.*, **84** (1998), p. 3530.
51) J. Haidar, *J. Appl. Phys.*, **85** (1998), p. 3448.
52) F.L. Zhu, H.L. Tsai, S.P. Marin and P.C. Wang, *Progress in Computational Fluid Dynamics*, **4** (2004), p. 99.
53) H.G. Fan and R. Kovacevic, *J. Phys. D: Appl. Phys.*, **37** (2004), p. 2531.
54) L.A. Jones, T.W. Eagar and J.H. Lang, *Welding J.*, (1998), p. 135s.
55) L.A. Jones, T.W. Eagar and J.H. Lang, *J. Phys. D: Appl. Phys.*, **31** (1998), p. 93.
56) L.A. Jones, T.W. Eagar and J.H. Lang, *J. Phys. D: Appl. Phys.*, **31** (1998), p. 107.
57) J. Hu and H.L. Tsai, *Int. J. Heat Mass Transfer*, (2006), submitted.
58) J. Hu and H.L. Tsai, *J. Appl. Phys.*, **100** (2006), in production.
59) J. Hu and H.L. Tsai, *J. Heat Transfer*, (2006) accepted.
60) H. Guo and H.L. Tsai, *Prco. Heat Transfer/Fluids engineering Summer Conference*, North Carolina (USA), American Society of Mechanical Engineering, July 11-15 (2004).
61) Y. Wang, Ph.D. Thesis, University of Missouri-Rolla, Rolla, Missouri, USA (1999).
62) AWS, *Welding handbook*, American Welding Society, 7th Edition, Vol. 2 (1983).
63) W.A. Baeslack, III, J.C. Lippold, and W.F. Savage: *Welding J.*, (1979), p.168s.
64) G. Speckhofer and H.P. Schmidt, *IEEE Trans. On Plasma Science*, **24**(1996), p. 1239.
65) Y.H. Kang and S.J. Na, *Welding J.*, (2002), p. 8s.